Acta Pharmaceutica Sinica B 2024;14(11):4858–4873

Chinese Pharmaceutical Association
Institute of Materia Medica, Chinese Academy of Medical Sciences

Acta Pharmaceutica Sinica B

www.elsevier.com/locate/apsb
www.sciencedirect.com

ORIGINAL ARTICLE

PPARα affects hepatic lipid homeostasis by perturbing necroptosis signals in the intestinal epithelium

Shufang Na[a,b], Yanjie Fan[a], HongLei Chen[c], Ling Li[b], Guolin Li[d], Furong Zhang[a], Rongyan Wang[a], Yafei Yang[a], Zixia Shen[a], Zhuang Peng[a], Yafei Wu[a], Yong Zhu[a], Zheqiong Yang[a], Guicheng Dong[e], Qifa Ye[b,*], Jiang Yue[a,f,*]

[a]*Department of Pharmacology, Taikang Medical School (School of Basic Medical Sciences), Wuhan University, Wuhan 430071, China*
[b]*Zhongnan Hospital of Wuhan University, Institute of Hepatobiliary Diseases of Wuhan University, Transplant Center of Wuhan University, National Quality Control Center for Donated Organ Procurement, Hubei Key Laboratory of Medical Technology on Transplantation, Hubei Provincial Clinical Research Center for Natural Polymer Biological Liver, Wuhan 430071, China*
[c]*Department of Pathology, Taikang Medical School (School of Basic Medical Sciences), Wuhan University, Wuhan 430071, China*
[d]*Center for Biomedical Aging, National & Local Joint Engineering Laboratory of Animal Peptide Drug Development, College of Life Sciences, Hunan Normal University, Changsha 410081, China*
[e]*College of Life Science, Inner Mongolia Agricultural University, Hohhot 010011, China*
[f]*Hubei Province Key Laboratory of Allergy and Immunology, Wuhan 430060, China*

Received 6 March 2024; received in revised form 6 June 2024; accepted 10 July 2024

KEY WORDS

Gut–liver axis;
NAFLD;
PPARα;
Intestine;
LPS;
Liver;

Abstract Rapid turnover of the intestinal epithelium is a critical strategy to balance the uptake of nutrients and defend against environmental insults, whereas inappropriate death promotes the spread of inflammation. PPARα is highly expressed in the small intestine and regulates the absorption of dietary lipids. However, as a key mediator of inflammation, the impact of intestinal PPARα signaling on cell death pathways is unknown. Here, we show that *Pparα* deficiency of intestinal epithelium up-regulates necroptosis signals, disrupts the gut vascular barrier, and promotes LPS translocation into the liver. Intestinal *Pparα* deficiency drives age-related hepatic steatosis and aggravates hepatic fibrosis induced by a high-fat plus

*Corresponding authors.
E-mail addresses: yqf_china@163.com (Qifa Ye), yuejiang@whu.edu.cn (Jiang Ue).

Peer review under the responsibility of Chinese Pharmaceutical Association and Institute of Materia Medica, Chinese Academy of Medical Sciences.

https://doi.org/10.1016/j.apsb.2024.08.021

Necroptosis;
Butyric acid

high-sucrose diet (HFHS). PPARα levels correlate with TRIM38 and MLKL in the human ileum. Inhibition of PPARα up-regulates necroptosis signals in the intestinal organoids triggered by TNF-α and LPS stimuli *via* TRIM38/TRIF and CREB3L3/MLKL pathways. Butyric acid ameliorates hepatic steatosis induced by intestinal *Pparα* deficiency through the inhibition of necroptosis. Our data suggest that intestinal PPARα is essential for the maintenance of microenvironmental homeostasis and the spread of inflammation *via* the gut−liver axis.

1. Introduction

The gut−liver axis has been well-documented to be involved in both non-alcoholic fatty liver disease (NAFLD) and alcoholic liver disease. A meta-analysis including 5620 patients with inflammatory bowel disease showed the prevalence of NAFLD was 27.5%, suggesting a close relationship between intestinal microecology and NAFLD[1]. PPARα is recognized as a druggable target for the treatment of metabolic disease symptoms (*e.g.*, dyslipidemia)[2]. PPARα is highly expressed in the small intestine and regulates diverse pathways including lipid metabolism, cell cycle, and immune response[3]. PPARα agonist WY14643 increases villus height[3], and *Pparα* deficiency in the intestine epithelium prevented the cold-induced villi elongation in the small intestine[4]. PPARs have also been documented to protect against inflammation in mouse models[5,6]. A recent study has shown that the intestine-derived HDL3 enriching with LPS-binding protein (LBP) detoxified LPS by forming HDL3−LBP−LPS complex and protected the liver from inflammation and fibrosis[7]. The core components of HDL including APOA1 and ABCA1 are downstream genes of PPARα[8,9].

In the small intestine, a rapid turnover of intestinal epithelium (3−5 days) is a critical strategy to balance the uptake of nutrients and defend against environmental insults. The crosstalk between cell death and inflammatory signaling pathways was confirmed by the molecular mechanisms of cell death decision-making[10]. Intestinal *Pparα* deficiency reduced crypt proliferation, indicated by the decrease in crypt budding in the $Ppar\alpha^{\Delta IE}$ organoids[4,11]. However, the influence of PPARα signaling on cell death pathways in the intestine epithelium is unclear.

In this work, we investigate the influence of intestinal PPARα on the spread of gut-derived inflammation and lipid metabolism in the liver. Our work demonstrates that *Pparα* deficiency of the intestinal epithelium up-regulated necroptosis signals and increased LPS translocation *via* the gut−liver axis in mice. Our work adds to the current knowledge on intestinal PPARα signaling in fatty liver diseases.

2. Material and method

2.1. Animal models

Pparα-floxed ($Ppar\alpha^{fl/fl}$) mice were kindly provided by Professor Dr. Frank Gonzalez[12], and *villin-cre* and *albumin-cre* mice were from Model Animal Research Center of Nanjing University. *Pparγ*-floxed ($Ppar\gamma^{fl/fl}$) mice were obtained from the Jackson Laboratory (Bar Harbor).

$Ppar\alpha^{fl/fl}$ mice and $Ppar\gamma^{fl/fl}$ mice were respectively crossed with *villin-cre* mice to generate the mice with intestine-specific deletion of *Pparα* ($Ppar\alpha^{\Delta IE}$) or *Pparγ* ($Ppar\gamma^{\Delta IE}$), and hepatocyte-specific *Pparα* deletion ($Ppar\alpha^{\Delta hep}$) mice were generated using *albumin-cre* mice. *Pparα* knockout ($Ppar\alpha^{-/-}$) mice were kindly provided by Dr. Guolin Li (Hunan Normal University). All the transgenic mice were on C57BL/6J background. Male C57BL/6J wild-type mice (20−22g) were supplied by the Experimental Animal Center (Hubei, China). All the animals were housed in SPF facilities at the Center for Animal Experiment Laboratory of Wuhan University.

For fructose exposure, male mice were treated with tap water or high-fructose corn syrup (HFCS) containing 45% glucose and 55% fructose for 14 days. For antibiotic treatment, male mice were given an antibiotic cocktail by oral gavage for 14 days[13]. Ampicillin (1 mg/mL), gentamicin (1 mg/mL), metronidazole (1 mg/mL), neomycin (1 mg/mL), and vancomycin (0.5 mg/mL) were solved in the autoclaved drinking water. For butyrate treatment, male mice were given butyrate (50 mg/mL bacitracin) in drinking water for 14 days and were monitored for body weight daily. For the high-fat plus high-sucrose diet (HFHS) diet study, male mice were fed ad libitum a standard chow diet or HFHS diet containing 20% protein, 50% carbohydrate (34% sucrose), and 21% fat (Beijing HFK Bio-Technology Co., Ltd.). For the short-term treatment, 6-week-old animals were fed with HFHS continuously for 4 weeks. For long-term treatment, 6-week-old animals were fed with HFHS continuously for 16 weeks. All mouse studies were carried out in accordance with protocols approved by the Animal Care Committee of Wuhan University (WP20220034).

To detect LPS translocation through the gut−liver axis, male mice were given the antibiotic cocktail for 3 days and then orally gavaged with 1 mg fluorescein isothiocyanate (FITC)-LPS (Xi'an ruixi Biological Technology Co.) or 0.2 mL LPS-gold-complexes after 2 h of fasting[14]. FITC-LPS translocation in the liver was monitored by fluorescence microscopy at 4 h after the treatment, and LPS-gold complexes in the hepatocytes were analyzed by transmission electron microscope. For conjugation of LPS (*E. coli* 055:B5, Biosharp) to the colloidal gold particles (20 nm, Xi'an ruixi Biological Technology Co.), 10 mg LPS dissolved in PBS was dropped into the colloidal gold solution (pH 7.4) while gently shaking. After shaking for 5 min, the excessive LPS was removed by centrifugation (14,000 × *g* for 10 min).

2.2. Human samples

The ileum samples from patients who underwent surgery for transverse colon cancer were obtained from the pathology archives at Zhongnan Hospital of Wuhan University. The paraffin-embedded normal ileum samples were deidentified and checked by 2 independent pathologists. The study was approved by the Medical Ethics Committee of Zhongnan Hospital of Wuhan

University (2023120) with a waiver of written informed consent. The samples were processed as described in the methods of tissue microarray and immunohistochemistry.

2.3. Histopathological analysis

Liver tissues were fixed in 4% paraformaldehyde and then embedded into paraffin. Intestine tissues were fixed in modified Bouin's fixative overnight and then washed to remove residual contents. The intestinal segments were coiled into Swiss rolls and then fixed in 4% paraformaldehyde for subsequent paraffin embedding and sectioning. The slices were stained with hematoxylin and eosin (H&E), Masson's trichrome staining, and alkaline phosphatase (AP) staining. For Oil Red O staining, freshly frozen liver tissues were cut into sections. After fixation with paraformaldehyde, the samples were stained with Oil Red O.

2.4. Analysis of metabolic phenotyping

The body weight curves of littermate mice were monitored daily from 4 to 33 weeks. The weekly food intake was calculated by the average daily food intake for 21 consecutive days. Data were normalized to the body weight of the mice. Fasting blood glucose was monitored from tail veins and using accu-chek blood glucose meters (Roche) after fasting overnight. For the glucose tolerance test, the mice were fasted for 16 h and given 10% glucose by gavage at a dose of 2 g/kg. Blood glucose levels were monitored separately at 0, 15, 30, 60, 90 and 120 min. The same batch of mice was set aside for testing after a week of recovery. For the insulin tolerance test, the mice were fasted for 2 h, and injected 0.75 U/kg insulin into the intraperitoneal, blood glucose levels were monitored at 0, 15, 30, 45 and 60 min.

2.5. Biochemical analysis

Serum alanine aminotransferase (ALT) and aspartate aminotransferase (AST) were assessed using commercial assay kits from Nanjing Jiancheng Bioengineering Institute (Nanjing, China). Total cholesterol (TC), triglyceride (TG), and glycerolipids (GL) levels in serum and liver were determined using assay kits according to the manufacturer's instructions (Applygen Technologies Inc.). LPS concentration in serum was detected using the kit produced by Xiamen Bioendo Technology. HDL-C levels in plasma were determined using the commercial kit (Applygen Technologies Inc.). Serum ApoA1 levels were assayed by an ELISA kit (Elabscience Biotechnology).

2.6. Real-time RT-PCR

Total RNA was extracted from tissues using TRIzol reagents (Takara). The quantity and quality of the total RNA were determined using a NanoDrop spectrophotometer (Qiagen). cDNA was synthesized from total RNA with a Hifair® II 1st Strand cDNA Synthesis Kit (Yeasen Biotechnology) and amplified with SYBR Green (Novoprotein) using a CFX Connect real-time PCR detection system (Bio-Rad). The sequences of primers are listed in Supporting Information Tables S1 and S2. The $2^{-\Delta\Delta CT}$ method was used to calculate the relative mRNA expression level after the normalization with GAPDH.

2.7. RNA-sequencing

Total RNA was extracted from liver and ileum tissues from $Ppar\alpha^{fl/fl}$ and $Ppar\alpha^{\Delta IE}$ mice using the TRIzol reagent. The poly-T oligo-attached magnetic beads were used to purify mRNA. After the fragmentation, cDNA was synthesized and repaired. Hieff NGS® DNA selection beads were used for purification and fragment selection. After PCR amplification and quantification, a single-stranded circular DNA was generated and amplified by a rolling circle amplification to construct sequencing libraries. The sequencing libraries were sequenced on DNBSEQ-T7 with the PE150 model (Bioyi Biotechnology).

Data analysis was performed by Bioyi Biotechnology Co., Ltd. The original data in FASTQ format were filtered using fastp (v0.21.0) software. The filtered reads were mapped to the reference genome using HISAT2 (v2.1.0.). To estimate the expression level, we use StringTie (v2.1.5) to produce reconstructions of genes followed by the normalization using the FPKM method. The differential expression of genes was analyzed by DESeq2 (v1.30.1). The clusterProfiler (v3.18.1) was used to perform GO and KEGG enrichment analyses. Gene Set Enrichment Analysis (GSEA) was performed to identify differentially expressed gene sets using the R software (version 3.2.0).

2.8. Transmission electron microscopy

Liver and ileum tissues from male $Ppar\alpha^{fl/fl}$ and $Ppar\alpha^{\Delta IE}$ mice were fixed with 2.5% glutaraldehyde for 2 h. Then, the samples were prepared with the support of the Research Center for Medicine and Structural Biology of Wuhan University. The images were captured at 80 kV on an HT7700 transmission electron microscope.

2.9. Immunohistochemistry

The paraffin-embedded samples were cut into sections and then blocked using 3% bovine serum albumin (BSA). After antigen retrieval using citrate buffer (pH 6.0) or tris-EDTA buffer (pH 8.0), the samples were incubated with a polyclonal rabbit anti-mouse TGF-β (1:100, #A11916, ABclonal), polyclonal rabbit anti-mouse α-SMA (1:100, #A1011, ABclonal), monoclonal mouse anti-mouse NRLP3 (1:100, #68102-1-Ig, Proteintech), polyclonal rabbit anti-mouse IL-1β (1:100, #GB11113-100, Servicebio Technology Co., Ltd.), polyclonal rabbit anti-mouse MLKL (1:100, #A13451, ABclonal), monoclonal rabbit anti-mouse cleaved-caspase 3 (1:500, #9664, CST), or polyclonal rabbit anti-mouse TRIF (1:200, #23288-1-AP, Proteintech). HRP polymer secondary donkey anti-rabbit IgG (H+L) (1:300-500, #AS038, ABclonal) or HRP polymer secondary donkey anti-mouse IgG (H+L) (1:300, #AS033, ABclonal) antibodies were used. DAB Substrate Kit (Abacm) was used for visualization, and an Olympus BX53 fluorescence microscope (Olympus Corporation) was used to capture images.

2.10. Immunofluorescence

For tissue sections, antigen retrieval was performed as described above and incubated with a primary antibody overnight at 4 °C. The primary antibodies were as follows: polyclonal rabbit anti-mouse F4/80 (1:100, #A1256, ABclonal), monoclonal rabbit anti-mouse CD14 (1:100, #A19011, ABclonal), polyclonal rabbit

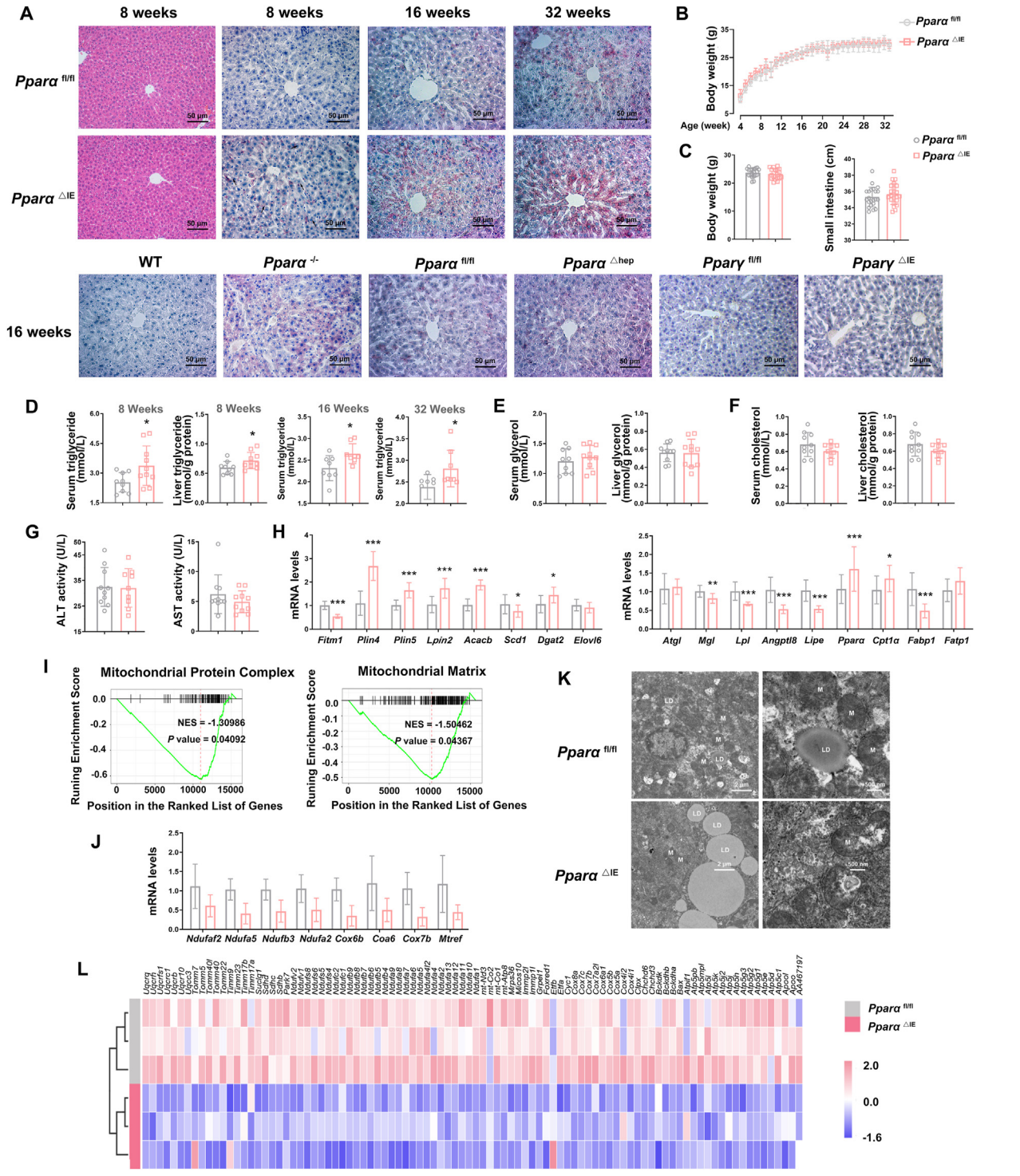

Figure 1 *Pparα* deficiency in intestinal epithelium promotes hepatic steatosis and mitochondria dysfunction in mice in a fed state. (A) Representative images of liver tissue stained with H&E and Oil Red O ($n = 5$). (B) Body weight of mice ($n = 8$). (C) Body weight, liver weight, and the length of the small intestine in 8-week-old mice ($n = 20$). (D) Triglyceride in serum and liver ($n = 10$). (E) Glycerol in serum and liver from 8-week-old mice ($n = 10$). (F) Cholesterol in serum and liver from 8-week-old mice ($n = 10$). (G) ALT, and AST in serum from 8- week-old mice ($n = 10$). (H) Relative mRNA levels of genes related with lipolysis, lipogenesis, and lipid droplet proteins in the liver from 8-week-old mice ($n = 5$). (I) GSEA analysis showing the changes in mitochondrial components in the liver from 8-week-old $Ppara^{\Delta IE}$ mice ($n = 3$). (J) Relative mRNA levels of genes related with mitochondrial components in the liver from 8-week-old mice ($n = 5$). (K) Transmission electron microscopy images of hepatocytes from 24-week-old mice ($n = 3$). (L) Heatmap representation of hepatic genes related with mitochondrial protein complex and matrix in 8-week-old $Ppara^{\Delta IE}$ relative to $Ppara^{fl/fl}$ ($n = 3$). LD: lipid droplet; M: mitochondria. Data are shown as the mean ± SD. An unpaired two-tailed Student's *t*-test; $^{*}P < 0.05$, $^{**}P < 0.01$, $^{***}P < 0.001$.

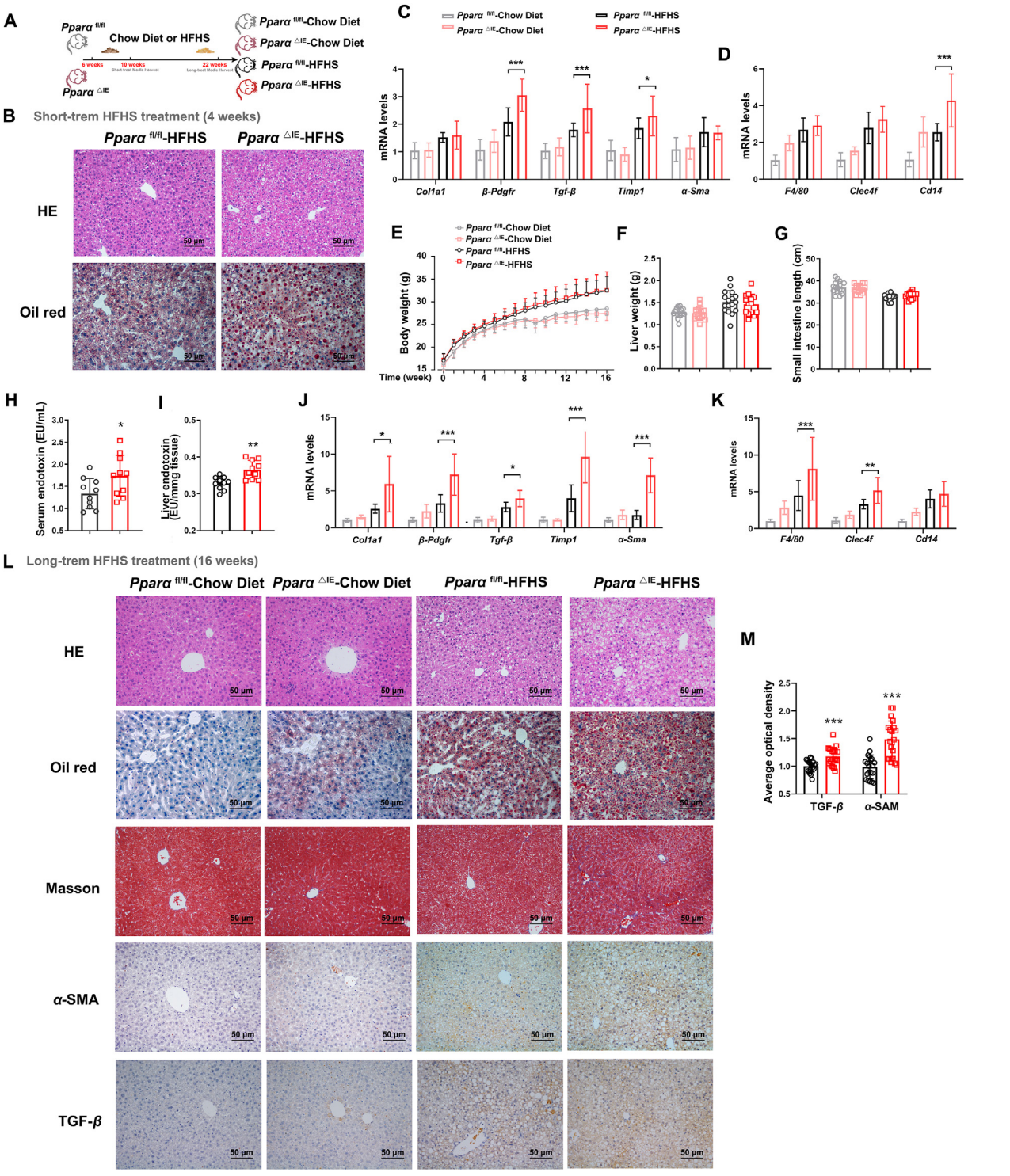

Figure 2 *Pparα* deficiency in intestinal epithelium promotes hepatic steatosis and fibrosis in mice fed a high-fat plus high-sucrose diet (HFHS). (A) Schematic representation of HFHS experimental design. (B) Representative images of liver tissue stained with H&E and Oil Red O after short-term HFHS treatment ($n = 5$). (C) Relative mRNA levels of *Col1a1*, *β-Pdgfr*, *Tgf-β*, and *Timp-1* in the liver after short-term HFHS treatment ($n = 5$). (D) Relative mRNA levels of *F4/80*, *Clec4f*, and *Cd14* in the liver after short-term HFHS treatment ($n = 5$). (E) Body weight of mice after long-term HFHS treatment ($n = 15$). (F) Liver weight of mice after long-term HFHS treatment ($n = 15$). (G) The length of the small intestine after long-term HFHS treatment ($n = 15$). (H) Serum endotoxin levels after long-term HFHS treatment ($n = 15$). (I) The endotoxin levels in the liver after long-term HFHS treatment ($n = 15$). (J) Relative mRNA levels of *F4/80*, *Clec4f*, and *Cd14* in the liver after short-term HFHS treatment ($n = 5$). (K) Relative mRNA levels of Col1a1, *β-Pdgfr*, *Tgf-β*, and *Timp1* in the liver after the HFHS treatment for 16 weeks ($n = 5$). (L) Representative images of liver tissue stained with H&E, Oil Red O, and Masson's trichrome and immunohistochemical staining for α-SMA and TGF-β after long-term HFHS treatment ($n = 5$). (M) Levels of α-SMA and TGF-β were quantified using Image J software and expressed as AODs. Data are shown as the mean ± SD. For the two groups, statistical significance was tested by unpaired Student's *t*-test; for more than two groups, statistical significance was tested by one-way ANOVA followed by the least significant difference (LSD) test; $^{*}P < 0.05$, $^{**}P < 0.01$, $^{***}P < 0.001$.

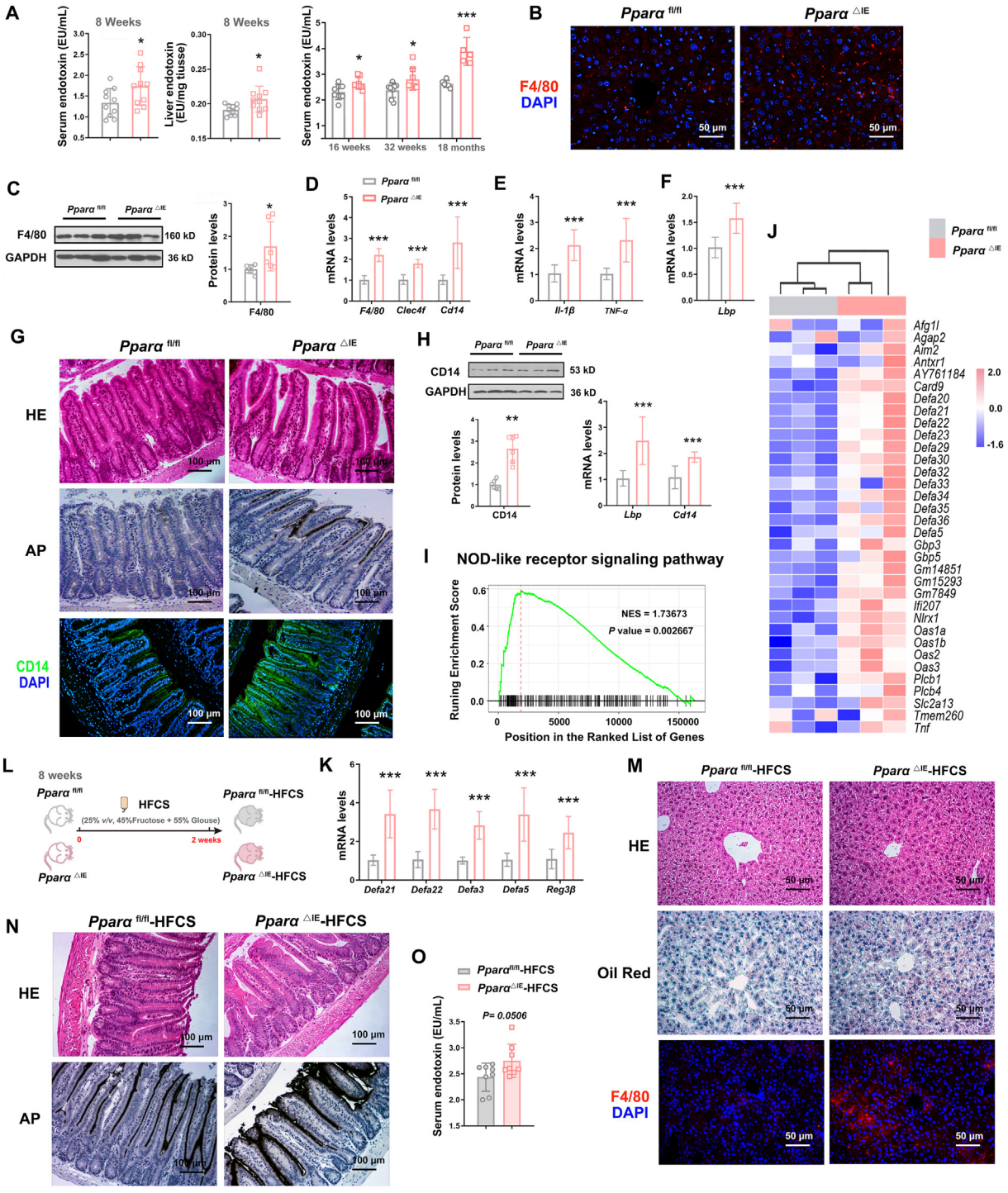

Figure 3 *Pparα* deficiency in intestinal epithelium activates inflammatory signaling pathways in both the ileum and liver. (A) Endotoxin in serum and liver ($n = 10$). (B) Immunofluorescent staining of F4/80 (red) in the liver of 8-week-old mice ($n = 5$). (C) Protein levels of F4/80 in the liver of 8-week-old mice ($n = 3$). (D) Relative mRNA levels of *F4/80*, *Clec4f*, and *Cd14* in the liver of 8-week-old mice ($n = 5$). (E) Relative mRNA levels of *Il-1β* and *Tnf-α* in the liver of 8-week-old mice ($n = 5$). (F) Relative mRNA levels of *Lbp* in the liver of 8-week-old mice ($n = 5$). (G) Representative H&E staining, immunohistochemical staining for AP, and immunofluorescent staining for CD14 (green) in the ileum of 8-week-old mice ($n = 5$). (H) Protein levels of CD14 and relative mRNA levels of *Lbp* and CD14 in the ileum of 8-week-old mice ($n = 5$). (I) Enrichment graph of NOD-like receptor signaling dataset performed with ileum samples from 8-week-old $Ppar\alpha^{\Delta IE}$ mice ($n = 3$). (J) Heatmap representation of genes involved in innate antibacterial defense in 8-week-old $Ppar\alpha^{\Delta IE}$ ileum relative to $Ppar\alpha^{fl/fl}$ ($n = 3$). (K) Relative mRNA levels of *Defa21*, *Defa22*, *Defa3*, *Defa5*, and *Reg3β* in the ileum from 8-week-old mice ($n = 5$). (L) Schematic representation of high-fructose corn syrup (HFCS) experimental design. (M) Representative images stained with H&E and Oil Red O, and immunofluorescent staining for F4/80 (red) in liver tissue from 8-week-old mice exposed to HFCS for 14 days ($n = 5$). (N) Representative H&E image and immunohistochemical staining for AP in the ileum of 8-week-old mice exposed to HFCS for 14 days ($n = 5$). (O) Serum endotoxin levels in 8-week-old mice exposed to HFCS for 14 days ($n = 8$). AP: alkaline phosphatase staining. Data are shown as the mean ± SD. An unpaired two-tailed Student's *t*-test; $^{*}P < 0.05$, $^{**}P < 0.01$, $^{***}P < 0.001$.

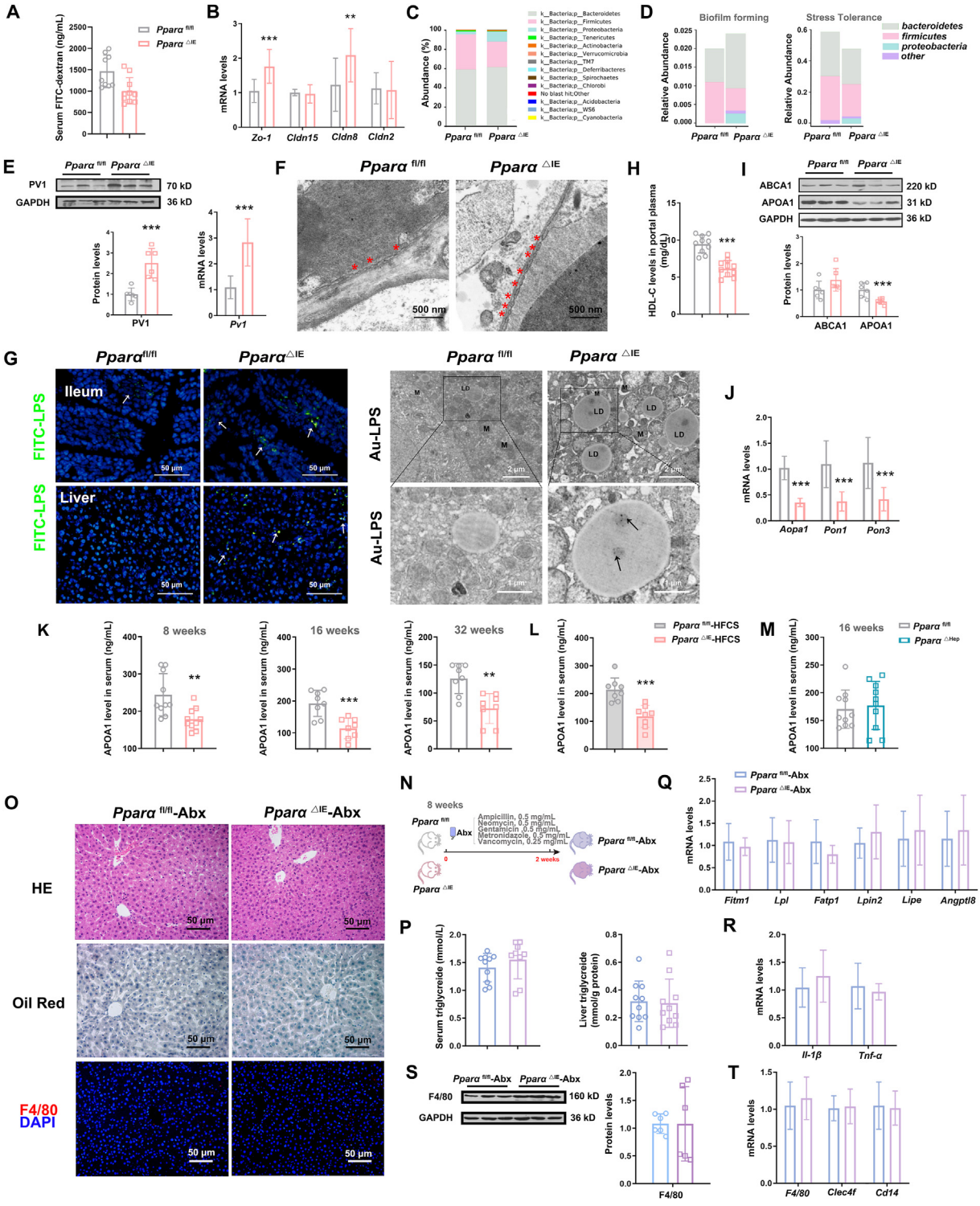

Figure 4 *Pparα* deficiency in intestinal epithelium increases the translocation of gut-derived antigens into the liver. (A) Intestinal permeability assessment (FITC-dextran, 4 kD) in 8-week-old mice ($n = 10$). (B) Relative mRNA levels of *Zo-1* and *Cldn8* in the ileum from 8-week-old mice ($n = 5$). (C) The relative proportion of bacterial species in the cecum content by 16S rRNA gene sequencing ($n = 6$). (D) Bugbase phenotypic prediction of gut microbiota in 8-week-old mice ($n = 6$). (E) The mRNA and protein levels of PV1 in the ileum of 8-week-old mice ($n = 5$). (F) Transmission electron microscopy images of the diaphragm (red star) in the capillaries from ileum sections in 24-week-old mice ($n = 3$). (G) Representative images of fluorescence microscopy and transmission electron in 8-week-old mice treated with FITC-LPS (green) or Au-LPS ($n = 3–5$). (H) Portal HDL-C levels in 8-week-old mice ($n = 10$). (I) The protein levels of APOA1 and ABCA1 in the ileum of 8-week-old mice ($n = 5$). (J) Relative mRNA levels of *Apoa1*, *Pon1*, and *Pon3* in the ileum of 8-week-old mice ($n = 5$). (K) Serum APOA1 levels in 8-, 16- and 32-week-old mice ($n = 8–10$). (L) Serum APOA1 levels in 8-week-old mice exposed to HFCS for 14 days ($n = 8$). (M) Serum APOA1 levels in 16-week-old $Ppar\alpha^{\Delta hep}$ mice ($n = 10$). (N) Schematic representation of a cocktail of broad-spectrum antibiotics (Abx) experimental design. (O)

anti-mouse FADD (1:100, #A20252, ABclonal), monoclonal rabbit anti-mouse p-RIPK3 (1:100, #91702, CST), monoclonal rabbit anti-mouse p-MLKL (1:200, #37333, CST), monoclonal rabbit anti-mouse cleaved-caspase 8 (1:100, #8592, CST), polyclonal rabbit anti-mouse TRIM38 (1:100, #13405-1-AP, Proteintech). Secondary antibodies included Alexa Fluor® 488 AffiniPure goat anti-rabbit IgG (H+L) (1:200-400, #111-545-003, Jackson ImmunoResearch) and Alexa Fluor® 594 AffiniPure goat anti-rabbit IgG (H+L) (1:200−1:400, #111-585-003, Jackson ImmunoResearch). The cell nuclei were labeled with DAPI. Images were captured using an Olympus BX53 fluorescence microscope (Olympus Corporation), and the settings for each image data set were identical.

2.11. Immunoblotting

Liver and ileum tissues were respectively homogenized in RIPA buffer containing protease inhibitor cocktail. The samples (10 μg protein) were separated by SDS-polyacrylamide gel electrophoresis and then transferred to PVDF membranes. These samples were incubated overnight with a polyclonal rabbit anti-mouse F4/80 (1:1000, #A1256, ABclonal), polyclonal rabbit anti-mouse APOA1 (1:2000, #A14211, ABclonal), polyclonal rabbit anti-mouse ABCA1 (1:1000, #NB400-105, Novus Biological, Centennial), monoclonal rabbit anti-mouse CD14 (1:1000, #A19011, ABclonal), or polyclonal rabbit anti-mouse PV1 (1:2000, #A15906, ABclonal). Monoclonal mouse anti-mouse GAPDH (1:5000, #AC002, ABclonal) was used as a loading control. Immunoblots were visualized by chemiluminescence and then exposed to autoradiographic film. The images were analyzed using a gel recording and analysis system (Beijing Liuyi Instruments).

2.12. Intestinal permeability test

Eight-week-old $Ppar\alpha^{\Delta IE}$ mice and $Ppar\alpha^{fl/fl}$ mice were used for the intestinal permeability test. The mice were given FITC-dextran (4 kD, 0.6 mg/g) by gavage after 6 h of fasting[15,16]. After the treatment for 4 h, the blood was collected and the serum was taken for the assay. PBS was used to dilute the serum and to create a standard curve. Multi-Mode Microplate Reader was used for the fluorescence assay with an excitation wavelength of 485 nm and an emission wavelength of 530 nm.

2.13. Gut bacteria metagenomic assay

Bacterial DNA from cecal contents was extracted using the E.Z.N.A Soil DNA Kit (OMEGA Bio-tek) followed by the quantity and quality using a NanoDrop spectrophotometer. Bacterial 16S rRNA genes were amplified by PCR using primers binding to the V3−V4 region. After purification of PCR products using VAHTSTM DNA Clean Beads (Vazyme), amplicon sequencing was performed on the Illumina MiSeq platform (paired-end) (Bioyi Biotechnology). Bioinformatic analysis was performed with QIIME2 (2019.4) and R software (version 3.2.0) by Bioyi Biotechnology Co., Ltd. Raw sequence data were demultiplexed using the demux plugin, and the DADA2 plugin was used to quality filter, denoise, merge and remove chimera. The classify-sklearn naïve Bayes taxonomy classifier was used to assign amplicon sequence variants (ASVs) to taxonomy categories. Alpha diversity analysis was performed using QIIME2, and the richness and evenness of ASVs were compared using abundance curves. LEfSe (Linear discriminant analysis effect size) was performed to determine differentially abundant taxa between $Ppar\alpha^{fl/fl}$ mice and $Ppar\alpha^{\Delta IE}$ mice. The phenotype analysis in microbiome samples was predicted using the BugBase platform (https://bugbase.cs.umn.edu).

2.14. Cell culture and treatment

HIEC-6 cells were transiently transfected with the PPARα and CREB3L3 expression vector for 24 h. To test the necroptosis signaling, HIEC-6 cells were treated with 30 ng/mL TNF-α for 24 h after the transfection with the PPARα and CREBL3 expression vector. HIEC-6 cells were exposed to butyric acid in the absence or presence of the selective PPARα inhibitor GW6471 (10 μmol/L) for 24 h.

2.15. Transient transfection and luciferase assay

The fragments encoding *PPARα* and *CREB3L3* were respectively cloned into the pSG5 vector and pcDNA3.1 (−) vector. The XhoI/HindIII fragment of the human TRIM38 promoter region (corresponding to region −2000, to +1 bp) was subcloned into the XhoI/HindIII digested pGL4.11 luciferase reporter vector. The XhoI/BglII fragment of the human *RIPK3* promoter region (−1500 to +1 bp) or *MLKL* promoter region (−2000 to +1 bp) was respectively subcloned into the XhoI/BglII digested pGL4.11 luciferase reporter vector. DNA sequence analysis was used to verify the constructs. To investigate the regulation of *TRIM38* by PPARα, HIEC-6 cells were transfected with *TRIM38* promoter reporter vector, phRL-TK *Renilla* luciferase control vector, PPARα expression plasmid, RXRα expression plasmid, or the empty vectors followed by the addition with WY14643 (10 μmol/L). To investigate the regulation of *RIPK3* and *MLKL* by CREB3L3, HIEC-6 cells were transfected with CREB3L3 expression plasmid, phRL-TK *Renilla* luciferase control vector, *RIPK3* promoter reporter vector, *MLKL* promoter reporter vector, or the empty vectors followed by the addition with GW6471 (10 μmol/L). After transfection for 24 h, luciferase activity was quantified using a dual-luciferase reporter assay system (Promega).

2.16. Intestinal organoid culture and treatment

Male 8-week-old mice were sacrificed and the ileum was removed and flushed 3 times with ice-cold PBS. The tissue was cut into segments and then washed with ice-cold PBS. The intestinal

Representative images stained with H&E and Oil Red O, and immunofluorescent staining for F4/80 (red) in the liver from 8-week-old mice treated with Abx ($n = 5$). (P) Triglyceride in serum and liver treated with Abx ($n = 10$). (Q) Relative mRNA levels of genes related to triglyceride accumulation in the liver from 8-week-old mice treated with Abx ($n = 5$). (R) Hepatic levels of cytokines from 8-week-old mice treated with Abx ($n = 5$). (S) Protein levels of F4/80 in the liver of 8-week-old mice treated with Abx ($n = 3$). (T) Relative mRNA levels of *F4/80, Clec4f*, and *Cd14* in the liver of 8-week-old mice treated with Abx ($n = 5$). LD: lipid droplet; M: mitochondria; FITC-LPS: fluorescein isothiocyanate (FITC)-LPS; Au-LPS: LPS-gold-complexes. Data are shown as the mean ± SD. An unpaired two-tailed Student's *t*-test; $^{**}P < 0.01$, $^{***}P < 0.001$.

crypts were isolated with Gentle Cell Dissociation Reagent (Stemcell Technologies) and filtered by a 70 μm cell strainer. After the quantification and centrifugation, the crypts were resuspended in IntestiCult™ Organoid Growth Medium (Stemcell Technologies) and mixed with Matrigel (Corning). The mixture containing 500 crypts was seeded in a pre-warmed 24-well plate and incubated at 37 °C for 10 min. After Matrigel polymerization, IntestiCult™ Organoid Growth Medium was added to each well and the cultures were incubated at 37 °C. Bright-field microscopy was used to monitor the development of intestinal crypts. To investigate the effect of PPARα on necroptosis, the organoid cultures were treated with TNF-α (30 ng/mL) and LPS (1 μg/mL) for 24 h after passing the organoid cultures[17].

2.17. Tissue microarray and immunohistochemistry

The tissue microarray of formalin-fixed and paraffin-embedded ileum samples was made by Servicebio Technology Co., Ltd. The sections were incubated with monoclonal mouse anti-human PPARα (1:200, #GTX22779, Genetex), polyclonal rabbit anti-human TRIM38 (1:100, #13405-1-AP, Proteintech), polyclonal rabbit anti-human MLKL (1:100, #A13451, ABclonal), monoclonal rabbit anti-human cleaved-caspase 3 (1:300, #9664, CST), polyclonal rabbit anti-human CD14 (1:100, #A19011, ABclonal), polyclonal rabbit anti-human FADD (1:100, #A20252, ABclonal), or polyclonal rabbit anti-human TRIF (1:200, #23288-1-AP, Proteintech) antibody overnight. HRP polymer secondary donkey anti-rabbit IgG (H+L) (1:300-500, #AS038, ABclonal) or HRP polymer secondary donkey anti-mouse IgG (H+L) (1:300, #AS033, ABclonal) antibodies were used to bind to the corresponding primary antibodies and DAB Substrate Kit was used for immunovisualization, three areas of each sample were randomly selected for image acquisition, and those with intact villi structures were further used for IHC scoring. Panoramic 1000 digital pathology scanner (3DHISTECH Ltd.), CaseViewer 2.4 (3DHISTECH Ltd), and Halo v3.0.311.314 (Indica labs) were used for IHC scoring.

2.18. Statistical analysis

Relative mRNA and protein levels were expressed as arbitrary units. Age- and sex-matched wild-type, $Ppar\alpha^{-/-}$, $Ppar\alpha^{fl/fl}$, $Ppar\alpha^{\Delta IE}$, $Ppar\gamma^{\Delta IE}$, and $Ppar\alpha^{\Delta hep}$ mice were assigned to groups without randomization. The data from *in vitro* experiments are shown as the mean ± standard error of mean (SEM) and the data from animal experiments were shown as the mean ± standard deviation (SD). The differences between the two groups were tested using an unpaired two-tailed Student's *t*-test. The differences among the groups were analyzed with one-way ANOVA followed by the least significant difference (LSD) test. Spearman's method was used to calculate the correlation coefficient for IHC scores of tissue microarrays. Differences with $P < 0.05$ were considered significant.

3. Results

3.1. Pparα deficiency of the intestinal epithelium drives age-related hepatic steatosis and mitochondria dysfunction in a fed state

Fat droplets were observed in liver tissue from 16-week-old *Pparα* knockout ($Ppar\alpha^{-/-}$) mice in a fed state when stained with Oil Red O (Fig. 1A). This is consistent with previous findings that $Ppar\alpha^{-/-}$ mice over 12 weeks of age had elevated plasma triglyceride levels and macrovesicular or large droplet fatty change in centrilobular hepatocytes in a fed state for unclear reason[18-20]. Age-related steatosis in centrilobular hepatocytes was also observed in intestine-specific deletion of *Pparα* ($Ppar\alpha^{\Delta IE}$) mice, but not in 16-week-old mice with hepatocyte-specific *Pparα* deletion ($Ppar\alpha^{\Delta hep}$) or intestine-specific *Pparγ* deletion ($Ppar\gamma^{\Delta IE}$) (Fig. 1A). The data suggest that the spontaneous lipid accumulation in the liver of $Ppar\alpha^{-/-}$ mice is not due to hepatic *Pparα* deletion, but rather to changes in intestinal PPARα levels. There were no differences in body weight, liver weight, and the length of the small intestine between $Ppar\alpha^{\Delta IE}$ mice and $Ppar\alpha^{fl/fl}$ mice (Fig. 1B and C). The triglyceride levels in serum and liver were slightly increased in $Ppar\alpha^{\Delta IE}$ mice compared with the control, while no changes in glycerol, cholesterol, and liver function were observed (Fig. 1D−G). The mRNA level of genes related to triglyceride synthesis (*Lpin2*, *Acacb*, and *Dgat2*) and lipid droplet-associated genes (*Plin4* and *Plin5*) were significantly up-regulated in $Ppar\alpha^{\Delta IE}$ liver compared with the control, while the genes related to lipolysis (*Mgl*, *Lpl*, *Lipe*, and *Angptl8*) were down-regulated (Fig. 1H). No significant differences in glucose tolerance and insulin tolerance were observed between $Ppar\alpha^{\Delta IE}$ mice and $Ppar\alpha^{fl/fl}$ mice (Supporting Information Fig. S1A and S1B). The levels of genes related to fatty acid metabolism in the liver were unchanged in $Ppar\alpha^{\Delta IE}$ mice after 24-h fasting compared with the control (Supporting Information Fig. S2).

GSEA of RNAseq data showed that intestinal *Pparα* deficiency caused the damage to mitochondrial protein complex and matrix in the liver (Fig. 1I and J). Electron microscopy revealed a massive lipid droplets accumulation, and mitochondria swelling as well as disruption of cristae in hepatocytes from 24-week-old $Ppar\alpha^{\Delta IE}$ mice, compared with the control (Fig. 1K). Heatmap depiction showed down-regulated genes in these two cellular components, including ATP synthases, ubiquinol-cytochrome *c* reductases, and mitochondrial ribosomal proteins in $Ppar\alpha^{\Delta IE}$ liver (Fig. 1L). The impaired ability of mitochondrial oxidative phosphorylation results in triglyceride accumulation in the hepatocytes[21]. These data suggest that the accumulation of lipid droplets in the hepatocytes caused by intestinal *Pparα* deficiency may be due to the impairment of mitochondrial function. The impairment of mitochondrial ultrastructure and functions (*e.g.*, ATP synthesis) has been observed in liver tissues of patients with obesity, non-alcoholic steatohepatitis, or various stages of alcoholic steatohepatitis[21].

3.2. Pparα deficiency of the intestinal epithelium accelerates hepatic fibrosis by HFHS

A high-fat diet plus fructose or sucrose markedly accelerated and aggravated fibrosis[22,23]. The experimental scheme is shown in Fig. 2A, with short-term treatment for HFHS lasting 4 weeks and long-term treatment lasting 16 weeks. We observed that the $Ppar\alpha^{\Delta IE}$ mice displayed aggravated hepatic steatosis after the short-term treatment of HFHS compared with the control (Fig. 2B). Fibrosis initiation was accelerated in the liver from $Ppar\alpha^{\Delta IE}$ mice after the short-term HFHS treatment compared with the control, indicated by the increased levels of marker genes (*β-Pdgfr*, *Tgf-β*, and *Timp-1*) (Fig. 2C); meanwhile, *Cd14* mRNA levels, a surface marker for hepatic macrophages, were increased in the $Ppar\alpha^{\Delta IE}$ mice (Fig. 2D). Weight gain, liver weight, and the length of the small intestine were unchanged between groups after long-term HFHS treatment (Fig. 2E−G).

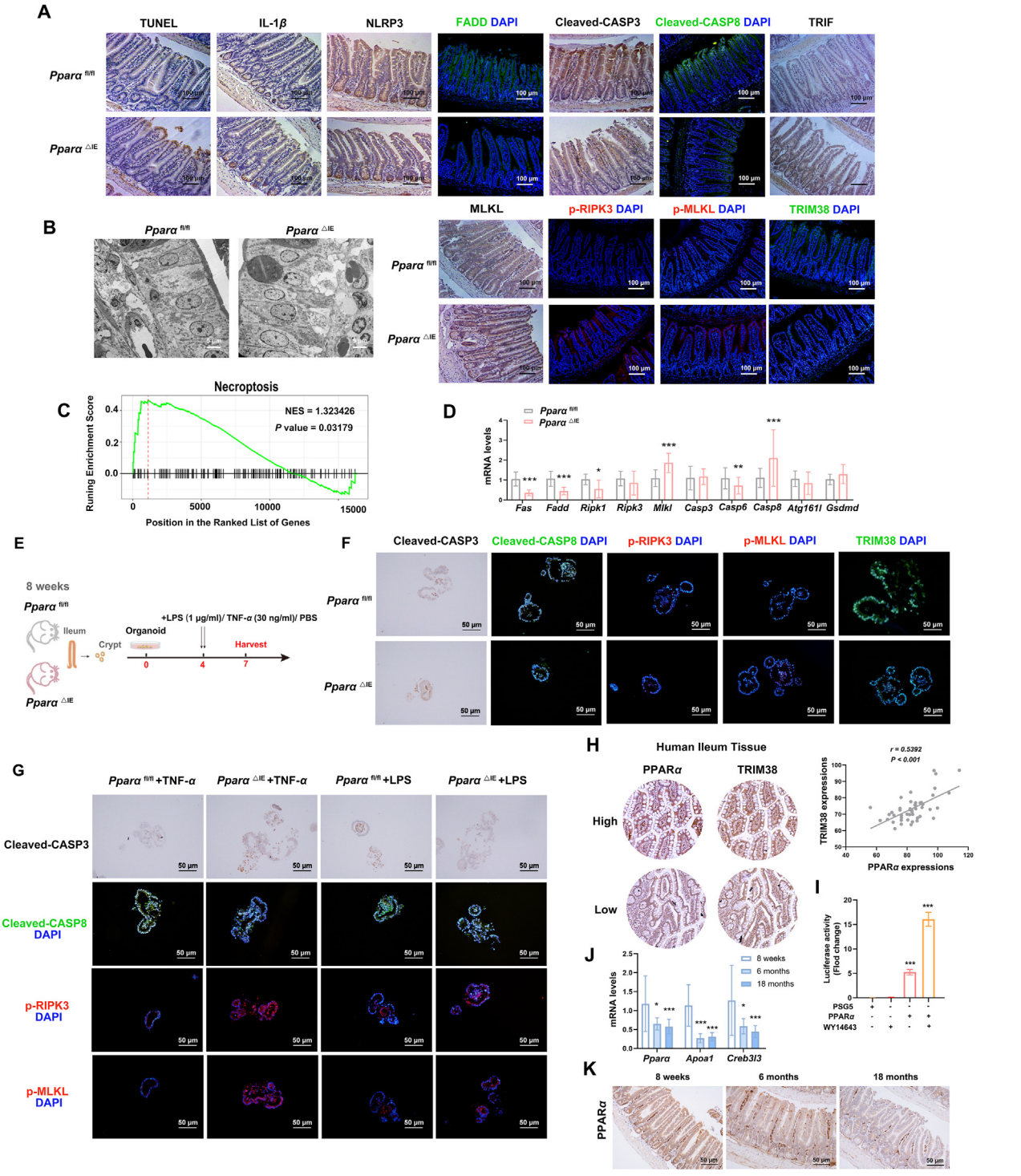

Figure 5 *Pparα* deficiency in intestinal epithelium up-regulates the necroptosis signaling pathway in the ileum from 8-week-old mice. (A) Representative TUNEL staining, immunohistochemical staining for IL-1β, NLRP3, cleaved-caspase 3, TRIF, and MLKL, and immunofluorescent staining for FADD (green), cleaved-caspase 8 (green), p-RIPK3 (red), p-MLKL (red), and TRIM38 (green) in the ileum ($n = 5$). (B) Transmission electron microscopy images of epithelial cells in the ileum from 24-week-old mice ($n = 3$). (C) Enrichment graph of necroptosis signaling dataset performed with ileum samples ($n = 3$). (D) Relative mRNA levels of genes related to apoptosis and necroptosis in ileum samples ($n = 5$). (E) Schematic representation of the experimental design using ileum organoid cultures from 8-week-old mice. (F) Immunofluorescent staining of apoptotic and necroptosis signaling components in organoid cultures ($n = 5$). (G) Immunofluorescent assay in ileum organoids treated with TNF-α and LPS ($n = 5$). (H) Spearman's method was used to analyze the correlation between PPARα expression and TRIM38 level in human ileum microarray ($n = 7$). (I) *TRIM38* promoter-driven luciferase activity in human intestinal epithelial HIEC-6 cells ($n = 3$). (J) Relative PPARα mRNA levels in mouse ileum ($n = 5$). (K) Representative immunohistochemical staining for PPARα in mouse ileum ($n = 5$). cleaved-CASP3: cleaved-caspase 3; cleaved-CASP8: cleaved-caspase 8. Data are shown as the mean ± SD. For the two groups, statistical significance was tested by unpaired Student's *t*-test; for more than two groups, statistical significance was tested by one-way ANOVA followed by the least significant difference (LSD) test; $^{*}P < 0.05$, $^{**}P < 0.01$, $^{***}P < 0.001$.

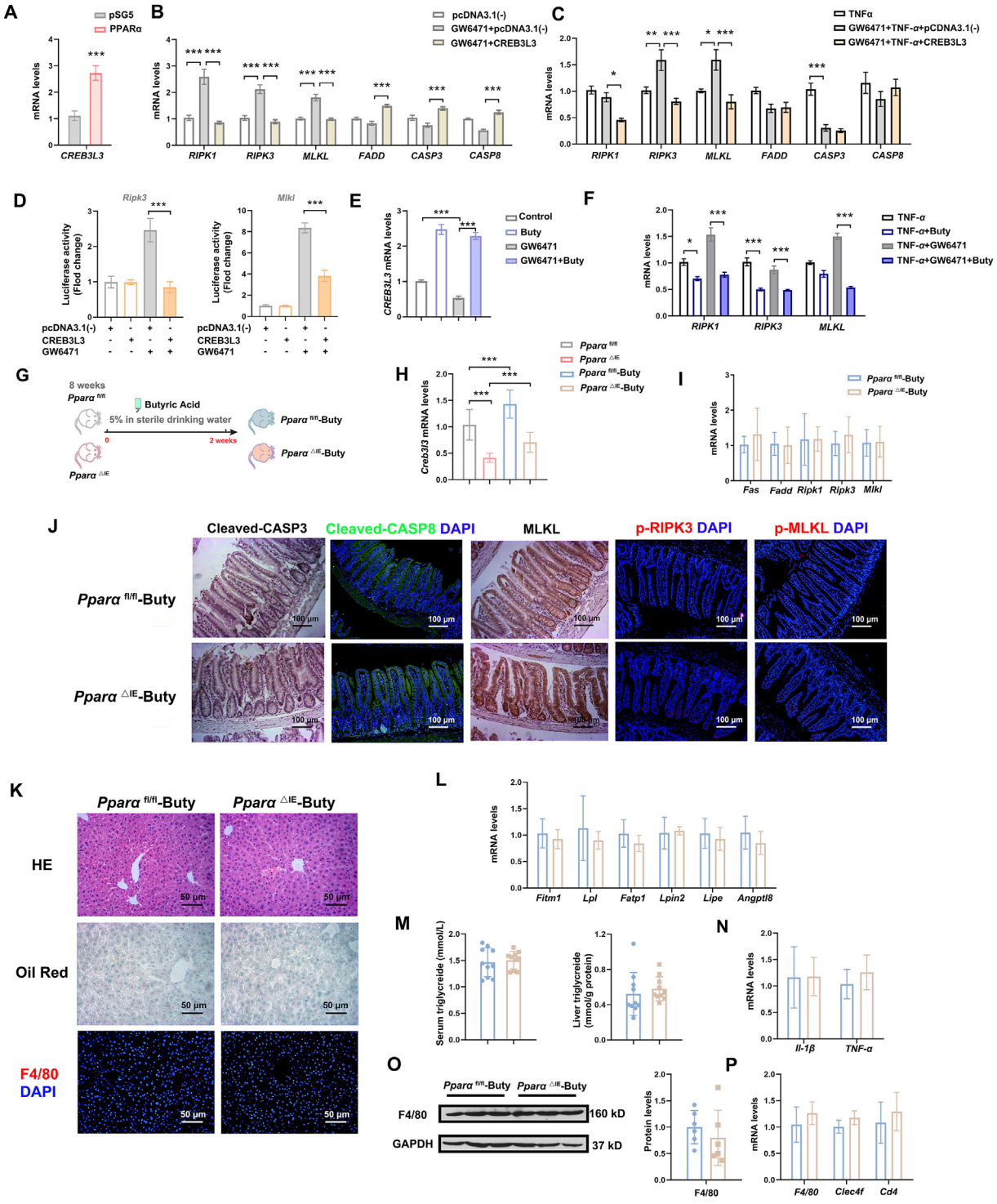

Figure 6 Butyric acid attenuates PPARα-induced necroptosis in HIEC-6 cells and ameliorates hepatic steatosis in *Pparα*$^{\Delta IE}$ mice. (A) Relative *CREB3L3* mRNA level in HIEC-6 cells transfected with the PPARα expression vector ($n = 3$). (B) Relative mRNA level of apoptotic and necroptosis signaling components in HIEC-6 cells transfected with the CREB3L3 expression vector ($n = 3$). (C) Relative mRNA level of apoptotic and necroptosis signaling components in HIEC-6 cells treated with TNF-α ($n = 3$). (D) Effects of GW6471 on *RIPK3* and *MLKL* promoter-driven luciferase activities in human intestinal epithelial HIEC-6 cells ($n = 3$). (E) Relative *CREB3L3* mRNA level in HIEC-6 cells treated with butyric acid ($n = 3$). (F) Relative mRNA level of necroptosis signaling components in HIEC-6 cells treated with TNF-α and butyric acid ($n = 3$). (G) Schematic representation of the experimental design for butyric acid treatment. H, Relative *CREB3L3* mRNA level in *Pparα*$^{fl/fl}$ and *Pparα*$^{\Delta IE}$ mice treated with butyric acid ($n = 5$). (I) Relative mRNA level of necroptosis signaling components in *Pparα*$^{\Delta IE}$ mice treated with butyric acid ($n = 5$). (J) Representative immunohistochemical staining for cleaved-caspase 3 and MLKL, and immunofluorescent staining for cleaved-caspase 8 (green), p-RIPK3 (red), and p-MLKL (red) in the ileum after butyric acid treatment ($n = 5$). (K) Representative images stained with H&E and Oil Red O, and immunofluorescent staining for F4/80 (red) in liver tissue after butyric acid treatment ($n = 5$). (L) Relative mRNA

Compared with the control, *Pparα*$^{\Delta IE}$ mice had higher levels of endotoxin in both serum and liver after long-term HFHS treatment (Fig. 2H and I). The levels of surface markers for hepatic macrophages including *F4/80* and *Clec4f* were higher in the *Pparα*$^{\Delta IE}$ mice than in the control (Fig. 2J); additionally, the degree of liver fibrosis was aggravated in the *Pparα*$^{\Delta IE}$ mice (Fig. 2K−M).

3.3. *Pparα deficiency of the intestinal epithelium leads to the up-regulation of inflammatory signals in both the liver and ileum*

Compared with the age-matched control, *Pparα*$^{\Delta IE}$ mice on a standard chow diet had higher levels of serum endotoxin (Fig. 3A). Compared with the control, the levels of surface markers for hepatic macrophages (*F4/80*, *Clec4f*, and *Cd14*) and cytokines (*Il-1β* and *Tnf-α*) were increased in 8-week-old *Pparα*$^{\Delta IE}$ mice. The higher F4/80 levels in the liver were also observed in *Pparα*$^{-/-}$ mice compared with the control (Supporting Information Fig. S3A). LBP binds to LPS and transfers to CD14, which controls TLR4-mediated endocytosis[24,25]. The increased *Lbp* levels were observed in *Pparα*$^{\Delta IE}$ liver compared with the control (Fig. 3B−F).

The increased levels of alkaline phosphatase (AP) that acted as a highly anti-inflammatory component of the intestinal barrier were observed in *Pparα*$^{\Delta IE}$ ileum compared with the control (Fig. 3G). This is consistent with the finding that AP levels were higher in *Pparα*$^{-/-}$ ileum than in the control (Fig. S3A). *Pparα*$^{\Delta IE}$ mice had higher levels of *Lbp* and CD14 in the ileum than the control, but CD14 levels in the duodenum and jejunum were comparable (Fig. 3G and H, Supporting Information Fig. S4). The higher CD14 levels in the ileum were also observed in *Pparα*$^{-/-}$ mice compared with the controls (Fig. S3A). GSEA of RNAseq data indicated the enhancement of NOD-like receptor signaling pathway caused by intestinal *Pparα* deficiency (Fig. 3I). The levels of genes involved in innate antibacterial defense including the α-defensin family (*Defa21*, *Defa22*, *Defa3*, and *Defa5*) and regeneration of islet-derived 3-β (*Reg3β*) were increased in *Pparα*$^{\Delta IE}$ ileum (Fig. 3J and K).

A previous study showed that the 2-week fructose exposure aggravated LPS-induced systemic inflammation in the absence of metabolic disorder[26]. After fructose exposure for 2 weeks (Fig. 3L), the levels of serum endotoxin and hepatic F4/80 were higher in 8-week-old *Pparα*$^{\Delta IE}$ mice than the control; additionally, the lipid accumulation in *Pparα*$^{\Delta IE}$ liver was increased (Fig. 3M and O). The levels of AP were markedly increased in the ileum from *Pparα*$^{\Delta IE}$ mice exposed to HFCS compared with the control (Fig. 3N).

3.4. *Pparα deficiency of the intestinal epithelium promotes the spread of inflammation via the gut−liver axis*

The disruption of the intestinal barrier is a critical pathological process in chronic liver inflammation triggered by gut-derived endotoxin[27]. No change in the permeability was found in 8-week-old *Pparα*$^{\Delta IE}$ mice using FITC-labeled dextroglucose (Fig. 4A), which was consistent with the previous finding[4]. *Pparα*$^{\Delta IE}$ mice had even higher levels of tight junctions (*Zo-1* and *Cldn8*) compared with the control (Fig. 4B).

The gut vascular barrier (GVB) controls the entrance of bacteria and bacterial products into the liver *via* the portal circulation, besides the intestinal epithelial barrier to prevent bacteria translocation[28]. The disruption of GVB has been found as an early event in NASH development. The extracellular structural domain of plasma vesicle-associated protein (PV1) forms a protein mesh that is arranged in chains of fine fibers as microscopic openings in the capillaries[29]. PV1 is a marker of GVB permeability, and its expression has been reported to be markedly up-regulated by LPS and a high-fat diet in the ileum[28]. The induction of PV1 leads to the increase in caveolae-mediated transcellular transport of endothelial cells[30]. The up-regulation of PV1 in the jejunum and ileum was correlated with the spread of *Salmonella* into the liver after oral infection[31]. The data from 16S rRNA gene amplicon sequencing in the cecum content showed an increased proportion of *Proteobacteria* in cecum contents from *Pparα*$^{\Delta IE}$ mice compared with the control; additionally, the abundance of *Proteobacteria* in biofilm-forming and stress-tolerant bacteria was higher in *Pparα*$^{\Delta IE}$ mice than in the control based on BugBase analysis (Fig. 4C and D). The expression levels of PV1 in the ileum from *Pparα*$^{\Delta IE}$ mice were increased compared with the control (Fig. 4E). Electron microscopy revealed that the microscopic openings in the capillaries were increased in ileum villi from *Pparα*$^{\Delta IE}$ mice compared with the control (Fig. 4F). FITC-LPS was sporadically detectable in the ileum villi from *Pparα*$^{fl/fl}$ mice, but not in the liver (Fig. 4G). However, the levels of FITC-LPS were significantly increased in both the ileum villi and liver in *Pparα*$^{\Delta IE}$ mice. Transmission electron microscopy showed the presence of LPS within lipid droplets of hepatocytes from *Pparα*$^{\Delta IE}$ mice, which was not observed in *Pparα*$^{fl/fl}$ mice.

Pparα$^{\Delta IE}$ mice had lower portal HDL-C levels compared with the control (Fig. 4H). The protein levels of APOA1 in *Pparα*$^{\Delta IE}$ ileum were lower than the control (Fig. 4I). *Pparα*$^{\Delta IE}$ mice had lower levels of serum APOA1 than the age-matched control, although an age-dependent reduction of serum APOA1 was observed (Fig. 4K). Serum APOA1 was reduced by short-term HFCS exposure in 8-week-old *Pparα*$^{\Delta IE}$ mice (Fig. 4L). No change in serum APOA1 levels was observed in 16-week-old *Pparα*$^{\Delta hep}$ mice compared with the control (Fig. 4M). Pon1 and Pon3 are associated with HDL particles and have antioxidant and anti-inflammatory actions. The mRNA levels of *Pon1* and *Pon3* in the ileum from 8-week-old *Pparα*$^{\Delta IE}$ mice were lower than the control (Fig. 4J).

We depleted the intestinal microbiota of 8-week-old *Pparα*$^{\Delta IE}$ mice using a cocktail of broad-spectrum antibiotics (Abx) (Fig. 4N). Lipid accumulation was undetectable in *Pparα*$^{\Delta IE}$ liver after Abx treatment (Fig. 4O); unsurprisingly, there was no difference in triglyceride levels in both serum and liver between *Pparα*$^{\Delta IE}$ mice and *Pparα*$^{fl/fl}$ mice (Fig. 4P). No difference in the expression of genes related to triglyceride synthesis (*Lpin2*), lipolysis (*Lpl* and *Angptl8*), lipid droplet-associated genes (*Plin4*

levels of genes related with lipolysis, lipogenesis, and lipid droplet proteins in the liver after butyric acid treatment ($n = 5$). (M) Triglyceride in serum and liver after butyric acid treatment ($n = 10$). (N) Hepatic levels of cytokines in mice after butyric acid treatment ($n = 5$). (O) Protein levels of F4/80 in the liver after butyric acid treatment ($n = 3$). (P) Relative mRNA levels of *F4/80*, *Clec4f*, and *Cd14* in the liver after butyric acid treatment ($n = 5$). Buty: butyric acid. Data are shown as the mean ± SD. For the two groups, statistical significance was tested by unpaired Student's *t*-test; for more than two groups, statistical significance was tested by one-way ANOVA followed by the least significant difference (LSD) test; $^{*}P < 0.05$, $^{**}P < 0.01$, $^{***}P < 0.001$.

and *Plin5*) was found between *Pparα*$^{\Delta IE}$ liver and *Pparα*$^{fl/fl}$ liver (Fig. 4Q). Additionally, the hepatic levels of surface markers of macrophages and cytokines were unchanged in *Pparα*$^{\Delta IE}$ mice treated with Abx compared with the control (Fig. 4R−T).

3.5. *Pparα deficiency of the intestinal epithelium affects the cell death pathway in the ileum*

We measured *in situ* cell death using TUNEL staining, and the data indicated that *Pparα* deficiency increased cell death at the top of the ileum villus (Fig. 5A). Although the *Pparα*$^{\Delta IE}$ mice had higher IL-1β levels in the ileum, no differences in NLRP3 levels were observed between the *Pparα*$^{\Delta IE}$ and *Pparα*$^{fl/fl}$ ileum (Fig. 5A). Electron microscopy revealed nuclear migration in columnar epithelia cells and heightened immune cell populations in the ileum from *Pparα*$^{\Delta IE}$ mice compared with the control (Fig. 5B), which is consistent with observations in patients with inflammatory bowel disease[32]. GSEA of RNAseq data indicated that intestinal *Pparα* deficiency caused the enrichment of the necroptosis signaling pathway in the intestine (Fig. 5C). Unlike apoptosis, necroptosis causes the leakage of soluble intracellular contents and the induction of proinflammatory responses[33]. Compared with the control, the expression levels of apoptotic signaling components (FAS, FADD, RIPK1) were decreased in the *Pparα*$^{\Delta IE}$ ileum; additionally, the levels of cleaved-caspase 3 and cleaved-caspase 8 were decreased in the *Pparα*$^{\Delta IE}$ ileum (Fig. 5A and D). The *Pparα*$^{\Delta IE}$ mice had higher levels of necroptosis signaling components including phosphor-RIPK3 and phosphor-MLKL in the ileum (Fig. 5A), which is consistent with the findings in the ileum from *Pparα*$^{-/-}$ mice (Fig. S3B). RIPK3 can be directly activated by TLR signaling *via* the critical adaptor TRIF[33]. TRIF levels were increased in the ileum from *Pparα*$^{\Delta IE}$ mice, compared with the control (Fig. 5A). TRIM38 degrades TRIF *via* the polyubiquitination-proteasome pathways, and *Trim38* deficiency has been shown to promote TLR3/4-mediated cytokine induction (*e.g.*, TNF-α) and cell death triggered by LPS[34]. The decreased levels of Trim38 were observed in the ileum from both *Pparα*$^{\Delta IE}$ and *Pparα*$^{-/-}$ mice, compared with the respective control (Fig. 5A, Fig. S4B).

We investigated the checkpoints of apoptosis and necroptosis in the organoids to avoid the impact of gut microbiota on cell death pathways (Fig. 5E). Consistently with *in vivo* data, TRIM38 levels were lower in the *Pparα*$^{\Delta IE}$ organoids than in controls (Fig. 5F). TNF-α triggers RIPK1/RIPK3-mediated programmed cell death pathways including both apoptosis and necroptosis, and LPS activates RIPK3-mediated necroptosis *via* the TLR−TRIF pathway[33]. Compared with the control, the levels of cleaved caspase 8 were markedly reduced in the *Pparα*$^{\Delta IE}$ organoids in response to TNF-α and LPS stimuli (Fig. 5F); additionally, the phosphorylation of RIPK3 and MLKL was markedly induced in the *Pparα*$^{\Delta IE}$ organoids (Fig. 5G). In human ileum samples, a significant correlation was found between PPARα expression and TRIM38, FADD, or MLKL levels (Fig. 5H, Supporting Information Fig. S5). The transfection of PPARα expression vector and WY14643 treatment induced the transcriptional activity of the TRIM38 promoter in HIEC-6 cells compared with the control (Fig. 5I). Additionally, PPARα levels were decreased in the ileum from older mice compared with younger mice, suggesting an increased risk of necroptosis in the intestinal epithelium with age (Fig. 5J and K).

3.6. *Butyric acid inhibits necroptosis of the ileum epithelium and ameliorates hepatic steatosis in Pparα*$^{\Delta IE}$ *mice*

CREB3L3 is highly expressed in the small intestine and regulates lipid metabolism as well as inflammatory responses triggered by infection[35]. Intestinal *Creb3l3* is a downstream target gene of *Pparα* indicated by RNA-seq analysis in mice (data not shown) and transfection experiment in HIEC-6 cells (Fig. 6A). A previous study has shown that the *Creb3l3* promoter contains a functional PPRE site located at −178 to −166 bp in HepG2 cells[36]. The induction of necroptosis signaling components (RIPK1, RIPK3, and MLKL) and the inhibition of apoptosis signaling components (FADD, Caspase-3, and Caspase-8) by GW6471 were attenuated by CREB3L3 overexpression in HIEC-6 cells (Fig. 6B). A previous study has shown that PPARα directly bound to the PPRE of *CREB3L3* promoter to increase the transcriptional activity[36].

In response to TNF-α stimuli, CREB3L3 overexpression attenuated the induction of necroptosis signaling components by the inhibition of PPARα signaling in HIEC-6 cells (Fig. 6C). The elevated transcriptional activity of *RIPK3* and *MLKL* by GW6471 was significantly inhibited by CREB3L3 overexpression (Fig. 6D). This is consistent with the previous finding that CREB overexpression counteracted the induction of the promoter activities of *RIPK1*, *RIPK3*, and *MLKL* by PCB-95[37]. Compared with the control, the inhibition of CREB3L3 by GW6471 was completely reversed by butyric acid (Fig. 6E). Butyric acid reversed the induction of *RIPK3* and *MLKL* by GW6471 in response to TNF-α stimuli (Fig. 6F).

We investigated the changes in necroptosis signaling in *Pparα*$^{\Delta IE}$ ileum after supplementation with sodium butyrate (Fig. 6G). *Creb3l3* levels were decreased in the *Pparα*$^{\Delta IE}$ ileum compared with *Pparα*$^{fl/fl}$ mice, while butyric acid attenuated the inhibition of *Creb3l3* by *Pparα deficiency* (Fig. 6H). Butyric acid attenuated the induction of MLKL and the inhibition of cleaved-caspase 8 in the *Pparα*$^{\Delta IE}$ ileum compared with the control (Fig. 6I and J). Lipid accumulation in the liver was undetectable in *Pparα*$^{\Delta IE}$ mice treated with butyric acid (Fig. 6K). No difference was found in hepatic triglyceride and in the levels of genes related to triglyceride synthesis, lipolysis, and lipid droplet between *Pparα*$^{\Delta IE}$ liver and *Pparα*$^{fl/fl}$ liver after butyric acid treatment (Fig. 6L and M). Butyric acid counteracted the activation of hepatic macrophages induced by *Pparα* deficiency (Fig. 6N−P).

4. Discussion

The present study has demonstrated that PPAR in the intestinal epithelium regulates cell death signals in response to environmental insults (*e.g.*, LPS) and acts as a gate controller for the spread of inflammation through the gut−liver axis. Although the inhibition of the intestinal *Pparα* decreases the absorption of dietary lipids, we provide direct evidence that *Pparα* deficiency of the intestinal epithelium led to the up-regulation of necroptosis signals and the translocation of LPS into the liver. Our data have shown that *Pparα* deficiency in the intestinal epithelium causes mitochondrial dysfunction in the hepatocytes, and accelerates hepatic steatosis or fibrosis induced by HFCS and HFHS.

The disruption of PPARα signaling in the intestine epithelium reduced FABP1-mediated fatty acid uptake[38], indicating that the inhibition of intestinal PPARα may improve diet-induced hepatic steatosis and obesity. However, intestinal PPARα plays a crucial role in preventing endotoxin translocation and diffusion. PPARα

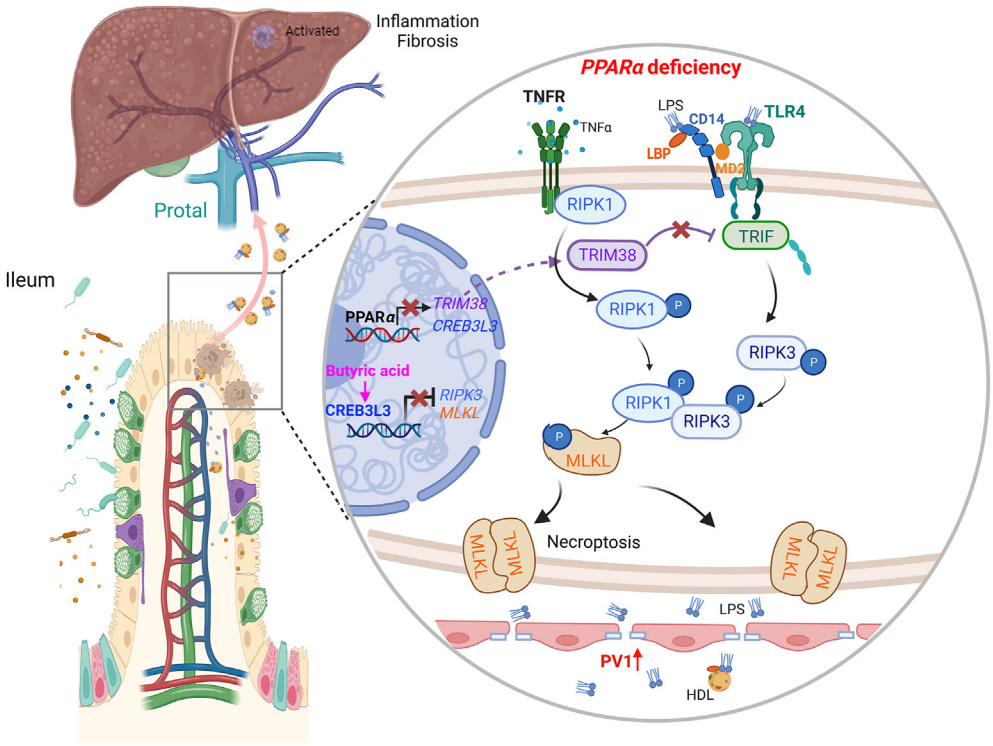

Figure 7 A model for the role of intestinal PPARα in maintaining microenvironmental homeostasis. PPARα deficiency up-regulates necroptosis signals in the ileum *via* TRIM38/TRIF and CREB3L3/MLKL pathways and promotes the spread of inflammation through gut−liver axis. Butyric acid may play a protective role against hepatic steatosis caused by PPARα deficiency of intestinal epithelium *via* the up-regulation of CREB3L3.

affects cell death processes in response to the stimuli in the small intestine. *Pparα* deficiency caused the enrichment of the necroptosis signaling pathway and heightened immune cell populations in the ileum. We found that PPARα regulated TRIF *via* TRIM38 as well as MLKL *via* CREB3L3, and that the deletion of PPARα promoted necroptosis triggered by TNFα or LPS. Intestinal *Pparα* deficiency increased LPS translocation into hepatocytes and impaired mitochondrial function. It is noteworthy that *Pparα* deficiency in the intestinal epithelium causes the spread of inflammation through GVB disruption, while the tight junction of the intestinal epithelial barrier is unchanged in $Ppar\alpha^{\Delta IE}$ mice.

Butyrate is a preferred metabolic substrate for intestinal epithelium and protects the intestinal barrier[39]. We found that *ex vivo* treatment of intestinal organoid cultures with butyric acid inhibited necroptosis signals (*e.g.*, total and phosphor-MLKL). The previous study has shown that butyrate directly increased intracellular cAMP levels and induced CREB phosphorylation through PKA signaling[40]. Butyric acid attenuated hepatic steatosis induced by *Pparα* deletion in the small intestine, and one possibility is that butyric acid inhibits necroptosis of the intestinal epithelium.

5. Conclusions

This study highlights that PPARα is essential to maintain homeostasis in the small intestine. The inappropriate cell death pathways of the intestinal epithelium induced by the alteration of PPARα signals could be one possible cause of hepatic steatosis. Interestingly, butyrate may play a protective effect against hepatosteatosis induced by intestinal *PPARα* deletion through the inhibition of necroptosis signals (Fig. 7). A comprehensive understanding of intestinal PPARα will be of significance for the development of new therapies for obesity and fatty liver disease.

Acknowledgments

This study was supported by the National Natural Science Foundation of China (Nos. 81673503 and 82204485), the China Postdoctoral Science Foundation (2022M712459), the Fundamental Research Funds for the Central Universities (2042022kf0022, China), the Joint Incubation Fund for Basic Medical and Clinical Research in Wuhan University (JCZN2022006, China), the Joint Foundation for Translational Medicine and Interdisciplinary Research in Zhongnan Hospital (ZNLH201903, ZNLH202319, China), Science and Technology Innovation Cultivation Fund of Zhongnan Hospital (CXPY2022083, China), the Program of Excellent Doctoral (Postdoctoral) of Zhongnan Hospital of Wuhan University (ZNYB20240002, China), and the 12th batch of grassland talents innovation and entrepreneurship talent team in Inner Mongolia (China).

Author contributions

Shufang Na: Writing − review & editing, Writing − original draft, Visualization, Validation, Methodology, Investigation, Funding acquisition, Formal analysis, Data curation, Conceptualization. Yanjie Fan: Methodology, Investigation, Formal analysis. HongLei Chen: Supervision, Investigation. Ling Li: Validation, Methodology, Investigation, Conceptualization. Guolin Li: Resources, Methodology. Furong Zhang: Visualization,

Validation, Methodology. Rongyan Wang: Validation, Methodology. Yafei Yang: Validation, Methodology, Formal analysis. Zixia Shen: Validation, Methodology. Zhuang Peng: Visualization, Validation, Investigation. Yafei Wu: Methodology, Investigation. Yong Zhu: Methodology, Investigation. Zheqiong Yang: Supervision, Methodology, Formal analysis. Guicheng Dong: Supervision, Funding acquisition, Formal analysis, Data curation. Qifa Ye: Supervision, Funding acquisition, Formal analysis, Data curation, Conceptualization. Jiang Yue: Writing − review & editing, Writing − original draft, Resources, Project administration, Methodology, Investigation, Funding acquisition, Formal analysis, Data curation, Conceptualization.

Conflicts of interest

The authors declare no conflicts of interest.

Appendix A. Supporting information

Supporting information to this article can be found online at https://doi.org/10.1016/j.apsb.2024.08.021.

References

1. Zou ZY, Shen B, Fan JG. Systematic review with meta-analysis: epidemiology of nonalcoholic fatty liver disease in patients with inflammatory bowel disease. *Inflamm Bowel Dis* 2019;**25**:1764−72.
2. Rigano D, Sirignano C, Taglialatela-Scafatin O. The potential of natural products for targeting PPARα. *Acta Pharm Sin B* 2017;**7**:427−38.
3. Bunger M, van den Bosch HM, van der Meijde J, Kersten S, Hooiveld GJ, Muller M. Genome-wide analysis of PPARalpha activation in murine small intestine. *Physiol Genomics* 2007;**30**:192−204.
4. Stojanovic O, Altirriba J, Rigo D, Spiljar M, Evrard E, Roska B, et al. Dietary excess regulates absorption and surface of gut epithelium through intestinal PPARalpha. *Nat Commun* 2021;**12**:7031.
5. Dubuquoy L, Rousseaux C, Thuru X, Peyrin-Biroulet L, Romano O, Chavatte P, et al. PPARgamma as a new therapeutic target in inflammatory bowel diseases. *Gut* 2006;**55**:1341−9.
6. Esposito G, Capoccia E, Turco F, Palumbo I, Lu J, Steardo A, et al. Palmitoylethanolamide improves colon inflammation through an enteric glia/toll like receptor 4-dependent PPAR-alpha activation. *Gut* 2014;**63**:1300−12.
7. Han YH, Onufer EJ, Huang LH, Sprung RW, Davidson WS, Czepielewski RS, et al. Enterically derived high-density lipoprotein restrains liver injury through the portal vein. *Science* 2021;**373**:eabe6729.
8. Gervois P, Torra IP, Fruchart JC, Staels B. Regulation of lipid and lipoprotein metabolism by PPAR activators. *Clin Chem Lab Med* 2000;**38**:3−11.
9. Ogata M, Tsujita M, Hossain MA, Akita N, Gonzalez FJ, Staels B, et al. On the mechanism for PPAR agonists to enhance *ABCA1* gene expression. *Atherosclerosis* 2009;**205**:413−9.
10. Patankar JV, Becker C. Cell death in the gut epithelium and implications for chronic inflammation. *Nat Rev Gastroenterol Hepatol* 2020;**17**:543−56.
11. Mana MD, Hussey AM, Tzouanas CN, Imada S, Barrera Millan Y, Bahceci D, et al. High-fat diet-activated fatty acid oxidation mediates intestinal stemness and tumorigenicity. *Cell Rep* 2021;**35**:109212.
12. Brocker CN, Yue J, Kim D, Qu A, Bonzo JA, Gonzalez FJ. Hepatocyte-specific PPARA expression exclusively promotes agonist-induced cell proliferation without influence from nonparenchymal cells. *Am J Physiol Gastrointest Liver Physiol* 2017;**312**:G283−99.
13. Dapito DH, Mencin A, Gwak GY, Pradere JP, Jang MK, Mederacke I, et al. Promotion of hepatocellular carcinoma by the intestinal microbiota and TLR4. *Cancer Cell* 2012;**21**:504−16.
14. Bárcena C, Valdés-Mas R, Mayoral P, Garabaya C, Durand S, Rodríguez F, et al. Healthspan and lifespan extension by fecal microbiota transplantation into progeroid mice. *Nat Med* 2019;**25**:1234−42.
15. Tambuwala MM, Cummins EP, Lenihan CR, Kiss J, Stauch M, Scholz CC, et al. Loss of prolyl hydroxylase-1 protects against colitis through reduced epithelial cell apoptosis and increased barrier function. *Gastroenterology* 2010;**139**:2093−101.
16. Aherne CM, Collins CB, Masterson JC, Tizzano M, Boyle TA, Westrich JA, et al. Neuronal guidance molecule netrin-1 attenuates inflammatory cell trafficking during acute experimental colitis. *Gut* 2012;**61**:695−705.
17. Lee C, An M, Joung JG, Park WY, Chang DK, Kim YH, et al. TNF-α induces LGR5+ stem cell dysfunction in patients with Crohn's disease. *Cell Mol Gastroenter* 2022;**13**:789−808.
18. Hashimoto T, Fujita T, Usuda N, Cook W, Qi C, Peters JM, et al. Peroxisomal and mitochondrial fatty acid beta-oxidation in mice nullizygous for both peroxisome proliferator-activated receptor alpha and peroxisomal fatty acyl-CoA oxidase. Genotype correlation with fatty liver phenotype. *J Biol Chem* 1999;**274**:19228−36.
19. Hashimoto T, Cook WS, Qi C, Yeldandi AV, Reddy JK, Rao MS. Defect in peroxisome proliferator-activated receptor alpha-inducible fatty acid oxidation determines the severity of hepatic steatosis in response to fasting. *J Biol Chem* 2000;**275**:28918−28.
20. Sanderson LM, Boekschoten MV, Desvergne B, Muller M, Kersten S. Transcriptional profiling reveals divergent roles of PPARalpha and PPARbeta/delta in regulation of gene expression in mouse liver. *Physiol Genomics* 2010;**41**:42−52.
21. Mansouri A, Gattolliat CH, Asselah T. Mitochondrial dysfunction and signaling in chronic liver diseases. *Gastroenterology* 2018;**155**:629−47.
22. Nevzorova YA, Boyer-Diaz Z, Cubero FJ, Gracia-Sancho J. Animal models for liver disease—a practical approach for translational research. *J Hepatol* 2020;**73**:423−40.
23. Simoes ICM, Karkucinska-Wieckowska A, Janikiewicz J, Szymanska S, Pronicki M, Dobrzyn P, et al. Western diet causes obesity-induced nonalcoholic fatty liver disease development by differentially compromising the autophagic response. *Antioxidants (Basel)* 2020;**9**:995.
24. Zanoni I, Ostuni R, Marek LR, Barresi S, Barbalat R, Barton GM, et al. CD14 controls the LPS-induced endocytosis of Toll-like receptor 4. *Cell* 2011;**147**:868−80.
25. Kim SJ, Kim HM. Dynamic lipopolysaccharide transfer cascade to TLR4/MD2 complex *via* LBP and CD14. *BMB Rep* 2017;**50**:55−7.
26. Jones N, Blagih J, Zani F, Rees A, Hill DG, Jenkins BJ, et al. Fructose reprogrammes glutamine-dependent oxidative metabolism to support LPS-induced inflammation. *Nat Commun* 2021;**12**:1209.
27. Albillos A, de Gottardi A, Rescigno M. The gut−liver axis in liver disease: pathophysiological basis for therapy. *J Hepatol* 2020;**72**:558−77.
28. Mouries J, Brescia P, Silvestri A, Spadoni I, Sorribas M, Wiest R, et al. Microbiota-driven gut vascular barrier disruption is a prerequisite for non-alcoholic steatohepatitis development. *J Hepatol* 2019;**71**:1216−28.
29. Chang TH, Hsieh FL, Gu XW, Smallwood PM, Kavran JM, Gabelli SB, et al. Structural insights into plasmalemma vesicle-associated protein (PLVAP): implications for vascular endothelial diaphragms and fenestrae. *Proc Natl Acad Sci U S A* 2023;**120**:e2221103120.
30. Wisniewska-Kruk J, van der Wijk AE, van Veen HA, Gorgels TG, Vogels IM, Versteeg D, et al. Plasmalemma vesicle-associated protein has a key role in blood−retinal barrier loss. *Am J Pathol* 2016;**186**:1044−54.
31. Spadoni I, Zagato E, Bertocchi A, Paolinelli R, Hot E, Di Sabatino A, et al. A gut−vascular barrier controls the systemic dissemination of bacteria. *Science* 2015;**350**:830−4.

32. Tachibana M, Tsutsumi Y. Colitis nucleomigrans: the third type of microscopic colitis (part 2). An ultrastructural study. *Pathol Int* 2020; **70**:761−6.
33. Ketelut-Carneiro N, Fitzgerald KA. Apoptosis, pyroptosis, and necroptosis—Oh my! The many ways a cell can die. *J Mol Biol* 2022; **434**:167378.
34. Hu MM, Xie XQ, Yang Q, Liao CY, Ye W, Lin H, et al. TRIM38 negatively regulates TLR3/4-mediated innate immune and inflammatory responses by two sequential and distinct mechanisms. *J Immunol* 2015;**195**:4415−25.
35. Khan HA, Margulies CE. The role of mammalian Creb3-like transcription factors in response to nutrients. *Front Genet* 2019;**10**:591.
36. Danno H, Ishii KA, Nakagawa Y, Mikami M, Yamamoto T, Yabe S, et al. The liver-enriched transcription factor CREBH is nutritionally regulated and activated by fatty acids and PPARalpha. *Biochem Biophys Res Commun* 2010;**391**:1222−7.
37. Guida N, Laudati G, Serani A, Mascolo L, Molinaro P, Montuori P, et al. The neurotoxicant PCB-95 by increasing the neuronal transcriptional repressor REST down-regulates caspase-8 and increases Ripk1, Ripk3 and MLKL expression determining necroptotic neuronal death. *Biochem Pharmacol* 2017;**142**:229−41.
38. Yan T, Luo Y, Yan N, Hamada K, Zhao N, Xia Y, et al. Intestinal peroxisome proliferator-activated receptor alpha-fatty acid-binding protein 1 axis modulates nonalcoholic steatohepatitis. *Hepatology* 2023;**77**:239−55.
39. Kelly CJ, Zheng L, Campbell EL, Saeedi B, Scholz CC, Bayless AJ, et al. Crosstalk between microbiota-derived short-chain fatty acids and intestinal epithelial HIF augments tissue barrier function. *Cell Host Microbe* 2015;**17**:662−71.
40. Wang A, Si H, Liu D, Jiang H. Butyrate activates the cAMP−protein kinase A−cAMP response element-binding protein signaling pathway in Caco-2 cells. *J Nutr* 2012;**142**:1−6.